

Experimental and Numerical Heat Transfer from Vortex-Injection Interaction in Scramjet Flowfields

Juan R. Llobet¹, Kevin D. Basore², Rowan J. Gollan³ and Ingo H. Jahn⁴

University of Queensland, Brisbane, QLD 4072, Australia

Air-breathing propulsion is expected to decrease the cost per kilogram for access-to-space while increasing the flexibility of available low earth orbits. However, improvements are required in order make this a reality, with one of the current issues under investigation being the effective fuel-air mixing inside of scramjet engines. A viable option suggested to address this issue uses the intrinsically generated vortices from scramjet inlets to enhance the downstream fuel-air mixing. Previous works have studied this vortex-injection interaction numerically, but the lack of published experimental data in the hypersonic regime made validation impractical. This paper extends upon these previous works by providing experimental data for the canonical geometry and assessing the numerical methodology to accurately predict the vortex-injection interaction.

To achieve this, an experimental model consisting of a flat plate with a perpendicular compression fin and a porthole injector was tested in the T4 Stalker Tube. The experimental data recorded was replicated numerically, allowing for the validation of the numerical methods. These results showed a localized overprediction of the heat transfer, attributed to a localized overprediction of the turbulent kinetic energy. Nonetheless, a good agreement was seen overall between the numerical and experimental results.

¹ PhD candidate, Centre for Hypersonics, School of Mechanical and Mining Engineering, j.r.llobet@uq.edu.au, Student Member AIAA.

² PhD candidate, Centre for Hypersonics, School of Mechanical and Mining Engineering, k.basore@uq.edu.au, Student Member AIAA.

³ Lecturer, Centre for Hypersonics, School of Mechanical and Mining Engineering, r.gollan@uq.edu.au, Member AIAA.

⁴ Lecturer, Centre for Hypersonics, School of Mechanical and Mining Engineering, i.jahn@uq.edu.au, Member AIAA.

I. Introduction

By removing the requirement of having to carry the propellant oxidizer, air-breathing propulsion has significant theoretical advantages over rockets. These advantages include, a higher specific impulse, efficiency, and payload mass fraction [1, 2]. For these reasons, using air-breathing propulsion for access-to-space missions has the potential to increase the overall efficiency of the missions as well as decrease the cost per kilogram of placing satellites into orbit. However, several aspects of scramjet technology still require substantial improvements prior to scramjet propulsion for access-to-space being considered operational. The extremely short residence times to mix and burn the fuel within these engines is one of the main challenges. A previously suggested strategy to enhance mixing while incurring a minimal total loss increase, is to use the vortices intrinsically generated by scramjet inlets. Non-axisymmetric inlets inherently generate vortices due to the shock-wave boundary-layer interactions present [3] and have been shown to produce improvements in mixing rates [4, 5]. A previous work [4] used RANS computational fluid dynamics (CFD) to study the vortex-injection interaction, focusing on its effect on fuel plume shape and its influence in mixing rate. These vortices were generated using a canonical geometry consisting of a flat plate and compression wall, which was previously shown to generate vortices representative of those found in real scramjet flowfields. This geometry is replicated in this experimental study to provide experimental data and a validation benchmark to assess the validity of numerical studies on this topic. The experiments are carried out in the T4 reflected shock tunnel at the University of Queensland (UQ).

II. T4 Reflected Shock Tunnel

The T4 is a reflected shock tunnel [6] at UQ.

III. Experimental Model

A simplified inlet geometry consisting of a flat plate with a normal fin at an angle of attack is used to generate scramjet-inlet-like vortices. This geometry and the flowfield it generates are

depicted in Fig. 1. The vortex is generated through shock-viscous interactions, similarly to the vortices generated by non-axisymmetric scramjet inlets [4, 7].

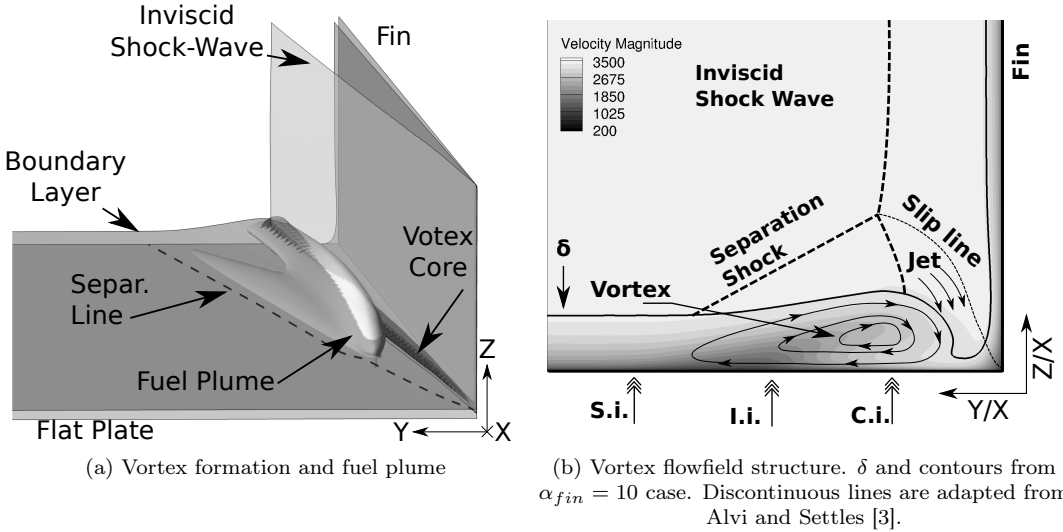


Fig. 1: Test geometry and vortex flowfield structure depiction. Extracted from [8]

The geometry used in the experimental campaign is equivalent to the one used in previous numerical works [4, 5, 7, 8], and is depicted in Fig. 2. The fin angle was 10° , selected for producing a relatively strong vortex withing an intensity representative of that of vortices present in real scramjet inlets [5, 7].

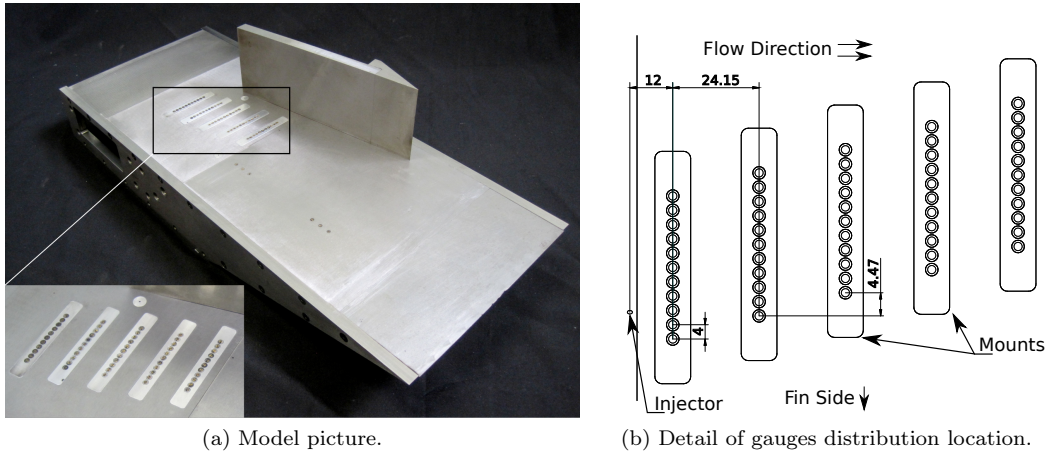


Fig. 2: Experimental model in its two configurations.

The width of the model, 220 mm was selected to avoid any influence of the side-wall 3D effects in the measurement region. The length of flat plate upstream of the fin leading edge was limited to 155.5 mm due to interference with the T4 tunnel nozzle walls. The location of the fin and injector

had to be adapted to the geometrical constraints of the test section and its optical accesses. The injector is located 125.7 mm downstream of the fin leading edge, with a size and angle of 1 mm and 45 deg respectively. The fin can be moved to allow different fin-to-injector distances, varying the location of the injector within the vortex.

Heat transfer measurements were obtained along five lines perpendicular to the axial direction. Data on each line is acquired using eleven thin film heat transfer gauges (TFHG). The thin films used in this experimental campaign were manufactured at the Centre for Hypersonics instrumentation laboratory. The metallic film is a 20 nm Nickel strip. The film is sputtered onto an optically smooth quartz substrate [9]. Nickel was chosen for its high temperature coefficient. The properties of Quartz vary very little with temperature, making it a good material for the substrate. In addition, these gauges are shielded with a layer of SiO_2 , reducing the wear of the film and avoiding possible short-circuits through an ionized flow [9]. The sensitivity of the gauges is calculated at the end of the manufacture process. The heat flux to the wall can be calculated using Eq. 1, from [9, 10], where $\rho c k_T$ are the properties of the substrate, and α_R is the TFHG sensitivity.

$$\dot{q}_n = \frac{\sqrt{\rho c k_T}}{\sqrt{\pi} \alpha_R V_0} \sum_{i=1}^n \frac{V(t_0) - V(t_{i-1})}{(t_n - t_i)^{1/2} + (t_n - t_{i-1})^{1/2}} \quad (1)$$

The gauges had to be mounted in close proximity to each other to provide the resolution required to reconstruct the heat transfer profile across the injection-vortex interaction region. The centers of the TFHG are separated 4 mm in the spanwise direction, while the lines are 24.15 mm apart in the axial direction. Moreover, the lines have a 4.47 mm offset between mounts in the spanwise direction as can be observed in Fig. 2b. The first TFHG line is 12 mm downstream of the injector.

Additionally, the model incorporates six thin film heat transfer gauges along the flat plate. These are used to identify the turbulent state of the flow in the vicinity of the fin leading edge and injector vicinity. These are grouped in two sets of three gauges 10 mm apart in the axial direction (Fig. 2a). The first set starts 143 mm from the flat plate leading edge. The central gauge is located at the same axial distance from the flat plate leading edge as the fin leading edge. The second set of

gauges starts 249 mm downstream of the flat plate leading edge. The last gauge in this set is located at an axial distance just upstream of the injector. These gauges are located away from the area of influence of the fin. Therefore, the measurements correspond to the boundary layer unaffected by the vortex. The boundary layer was found to remain laminar for the test conditions.

Two pressure tabs on the flat plate surface incorporating kulite pressure transducers were used to ascertain the pressure of the freestream.

A. T4 test flow conditions

The experiments were performed using the T4 Mach 7.6 nozzle and Mach 8 enthalpy conditions. The flow conditions at the nozzle exit are derived from measurements of the shock tube fill pressure (P_{ST}), shock tube shock speed (V_S), Shock tube temperature (T_{ST}), and nozzle supply pressure (P_e). Moreover, the transition onset location on the T4 nozzle wall surface is required. The length at which transition takes place is unknown. For this reason, a parametric study was performed, varying this parameter until the static pressure at the nozzle exit closely matched the experimental pressure measured on the flat plate.

The nozzle exit values are tabulated along with their uncertainties in Table 1.

Table 1: Nominal conditions during testing a nozzle exit.

Variable	Value
P_0 [MPa]	$15.74 \pm 4.42\%$
P_∞ [kPa]	$2.29 \pm 4.53\%$
T_∞ [K]	$237.24 \pm 7.37\%$
ρ_∞ [kg m^{-3}]	$0.0335 \pm 6.97\%$
u_∞ [m s^{-1}]	$2342.23 \pm 2.98\%$
M_∞ [-]	$7.57 \pm 0.70\%$
H_0 [MJ kg^{-1}]	$2.73 \pm 7.10\%$

The nozzle exit values Table 1 are calculated using NENZFr. NENZFr [11] is a set of scripts that coordinate a space-marched nozzle simulation in the CFD code Eilmer3, developed at University of Queensland. Eilmer3 is a collection of programs simulating 2-D/3-D Navier-Stokes transient compressible flow [12, 13]. It is specialised in solving accurately the flow in reflected shock tunnels and expansion shock tunnels. The equations are solved using an upwind scheme. Moreover, it calculates thermochemistry and finite-rate chemistry processes within the flowfield.

The grid used in the nozzle calculation is a 2-D grid, constructed by inscribing a uniform structured grid between a Bezier curve defining the nozzle wall and the axis of the nozzle. The mesh employed in this study consisted of 600 by 40 elements in the axial and radial directions respectively. The chemical composition of the gas is calculated using finite-rate reactions with a five species gas model: N_2 , O_2 , NO, N and O. The thermodynamic properties are obtained using the NASA CEA2 program [13, 14].

IV. Test cases

Two fin locations measured as the minimum spanwise distance between the fin and the injector center with respect to the injector are used. These correspond to fin-to-injector distances of 26.2 mm and 35.2 mm, and are named upper fin (UF), and lower fin (LF) positions respectively.

Hydrogen fuel is injected through a 1 mm diameter injector inclined 45° in the axial direction. Injection pressure is maintained constant during the test time using a Ludwieg tube. The injection pressures used are $P_{inj} = 1300 \text{ kPa}$ and $P_{inj} = 430 \text{ kPa}$, which are named high injection pressure (HI) and low injection pressure (LI) respectively. These pressures produce an injection-to-freestream injection momentum ratio of 5.24, and 1.73 respectively. The case with no injection (NI) is used to obtain heat flux data of the undisturbed vortex. These parameters are combined to produce 6 different test cases summarized in Table 2 .

Table 2: Combination of injection pressure and fin position for the different test cases.

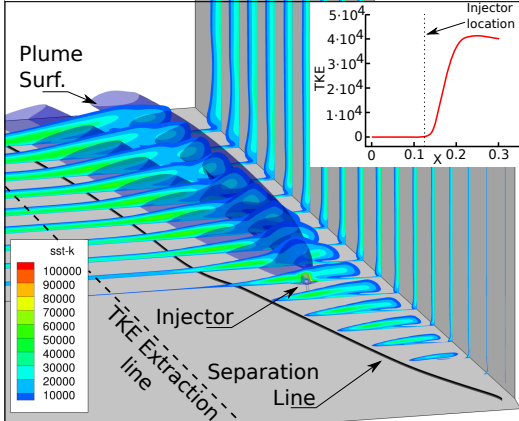
#	Naming	Injection Pressure	Fin-to-injector distance
1	NI-UF	- (-)	26.2 mm
2	NI-LF	- (-)	35.2 mm
3	HI-UF	$1300 \text{ kPa} \pm 3.1\%$	26.2 mm
4	LI-UF	$430 \text{ kPa} \pm 2.8\%$	26.2 mm
5	HI-LF	$1300 \text{ kPa} \pm 3.1\%$	35.2 mm
6	LI-LF	$430 \text{ kPa} \pm 2.8\%$	35.2 mm

V. CFD reference results

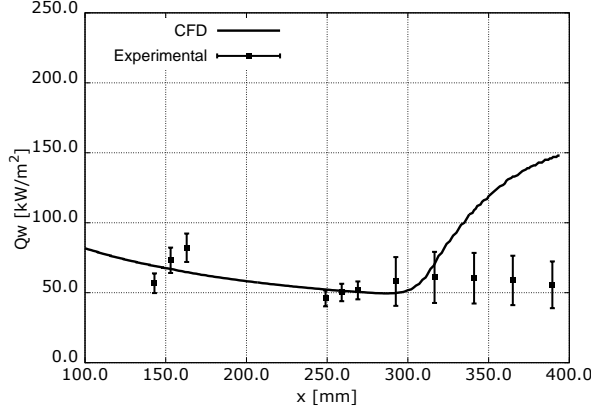
The data obtained in the experiments is complemented with numerical simulations to enhance the understanding of the results, and assess the validity of the numerical methodology. The numeri-

cal domain spans from 10 mm upstream of the fin leading edge, to 300 mm downstream, and 200 mm in the spanwise direction. The boundary layer development over the first 145.5 mm of flat plate upstream of the fin leading edge is calculated on a separated quasi 2-D simulation with an infinitely sharp leading edge, and used as the inflow for the main 3-D flow calculations. The 3-D mesh size is approximately 4 million cells. Within the injector vicinity, the cells size is approximately 0.05 mm, expanding up to 1 mm in the region of uniform flow, far from the vortex-injection interaction. The injector is placed at $X = 125$ mm downstream of the fin leading edge to match the experimental model. In the spanwise direction, the injector is placed at $Y = 26.2$ mm from the fin leading edge in the Upper fin position case, and $Y = 35.2$ mm in the Lower fin position. The walls are modeled as constant temperature non-slip walls, with a temperature of 300 K.

The inflow conditions for this simulation are the nominal conditions at the nozzle exit in Table 1. As transition is only anticipated downstream of the oblique shock and injector, the pseudo-2D simulations are performed as fully laminar. The main 3-D simulations of the flat plate plus fin are performed with the SST $k - \omega$ model to allow turbulent mixing of the fuel, and production of turbulence in the boundary layer region separated by the fin shock. To achieve this, the turbulence parameters are incorporated to the laminar inflow data with a value of zero at the domain inflow. In this manner, the laminar nature of the flow in the experiments is replicated for most of the flat plate in the numerical simulations. Most importantly, the combination of the laminar inflow with the SST $k - \omega$ model computation produces an effectively laminar boundary layer interaction with the fin shock, while allowing the generation of turbulence in the separation and injection regions. This can be observed in Fig. 3a. The turbulent kinetic energy remains almost negligible in the initial part of the domain, and only starts growing rapidly slightly downstream of the injector region. Thanks to the delayed onset of turbulent kinetic energy growth, the flow relevant for the region of interest remains laminar until its separation, qualitatively representing the turbulence state of the flow in the experimental case. The good agreement between the numerical and experimental flow conditions in the fully laminar region is depicted in Fig 3b.



(a) Turbulent kinetic energy (TKE) evolution in the numerical case.



(b) Experimental and numerical heat flux on the undisturbed flat plate region.

Fig. 3: Boundary layer state comparison between the experimental and numerical cases

VI. Results

The experimental and numerical data obtained is presented in this section. The case with no injection is presented first, followed by the study of the vortex-injection cases.

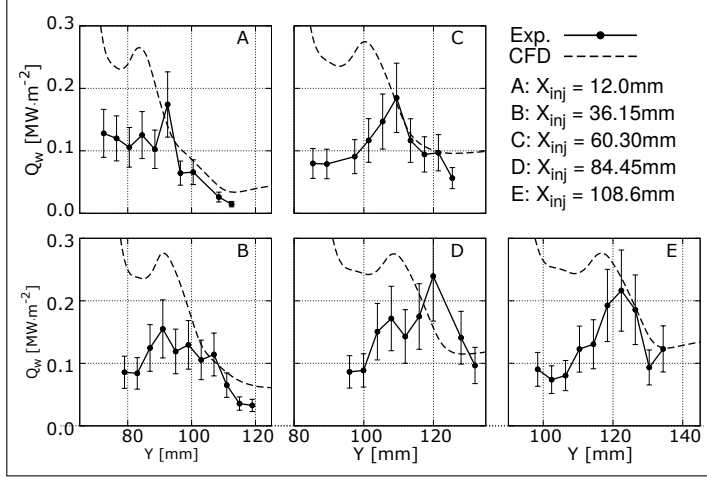
A. Unfueled vortex

Two tests using the the Upper and Lower fin positions with no injection were performed to identify the effect of the vortex on heat flux, and the ability of the numerical methodology to accurately simulate this flowfield.

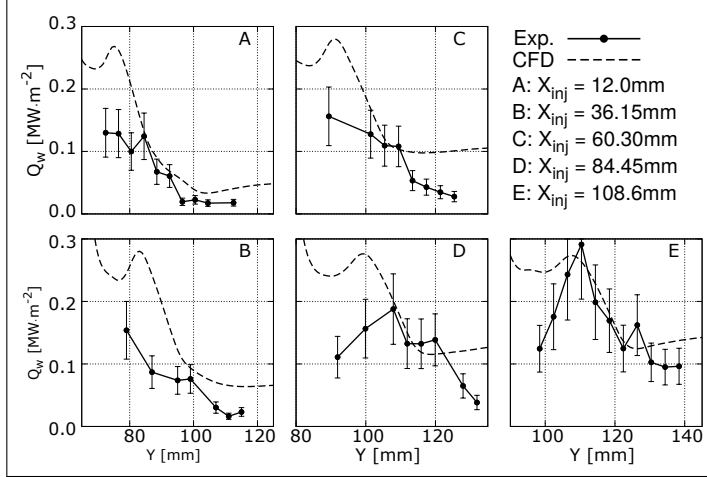
The experimental data along the lines formed by the gauges on each mount are presented in Fig. 4a and Fig. 4b for the Upper and Lower fin positions respectively.

The right hand side of the curves in both figures shows a relatively accurate match between the heat flux in the experimental and numerical cases. However, in the region closest to the fin shock (Low Y values), the heat flux is highly overestimated in the numerical results. This overestimation is consistent for all lines. Moreover, the Upper fin case presents a more prominent mismatch in this region. The region of numerically overestimated heat flux lies in the region closer to the fin shock. This can be seen in Fig. 5, which presents a mapped version of the data in Fig. 4b along with the equivalent numerical data map.

In the Lower fin position case, the fin is placed further from the gauge data acquisition region.



(a) Upper fin position.

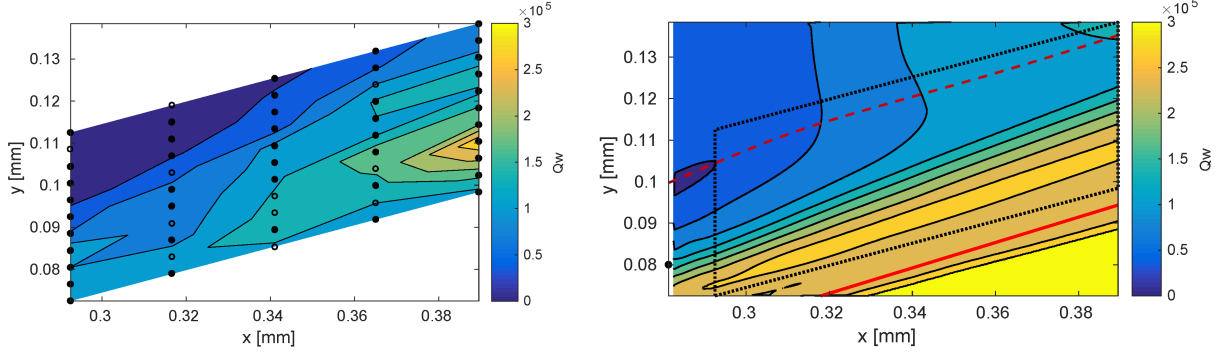


(b) Lower fin position.

Fig. 4: Numerical and experimental data on gauges lines A to E, at X_{inj} axial distance from the injector. Unfuelled vortex cases.

Therefore, a smaller part of the numerically overpredicted heat flux region is measured experimentally, reducing the discrepancy within the measurement region.

The vortex flowfield contains a separation and a reattachment line. The reattachment takes place behind the fin shock, driving hot and dense shock processed gas towards the flat plate, as observed in Fig 1b marked as 'jet'. This reattachment takes place in the region of numerically overestimated heat flux. Assuming the temperature of the gas and its composition after being processed by the fin shock are accurately predicted numerically, the overestimation of heat flux seems to be caused by an overestimation of the turbulence intensity in the reattachment region. This can be observed in Fig. 6. This figure shows line A from the Upper fin case (Fig. 4a) combined



(a) Experimental heat flux map. Solid dots are active gauges. Hollow dots are discarded gauges.
(b) Numerical heat flux map. Dotted line indicates experimental acquisition area. Dashed red line indicates separation line. Solid red line indicates location of inviscid fin shock.

Fig. 5: Reconstructed heat transfer map. Comparison of heat flux from experiments and CFD. NI-LF (Case 2 in Table 2).

with the turbulent kinetic energy at the same axial location extracted from the numerical data.

The location where the numerical overestimation becomes severe is coincident with the start of a region of high turbulent kinetic energy adjacent to the flat plate surface. The detail image in Fig. 6 clearly shows this region. The coincidence between the overestimation area with the high turbulent kinetic energy adjacent to the flat plate suggests the turbulence model is overpredicting turbulence and thus heat flux in this region.

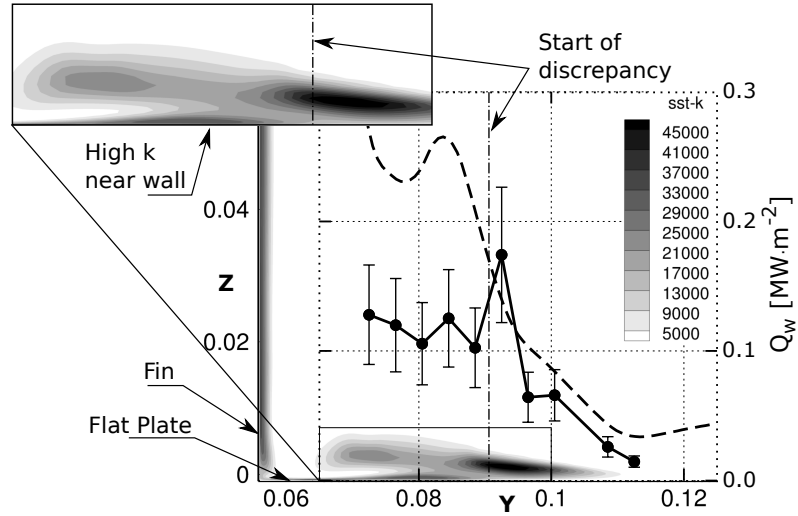


Fig. 6: Contours of turbulent kinetic energy combined with experimental and numerical heat flux at $X_{inj} = 12$ mm.

The limitation of the numerical model to accurately simulate heat flux near the fin shock is a key aspect to take into account when comparing the numerical and experimental results for the

fueled cases. This region of severe heat flux overprediction in the numerical data will be referred as ‘numerical overestimation zone’.

B. Fuel vortex interaction

The results obtained for the tests using the Upper and Lower fin positions in combination with the high and low injection pressures (cases 1-4 in Table 2) provide data on the complex vortex-injection interaction flow field.

1. Upper fin position, High injection pressure

Both the experimental and numerical results for the high injection pressure and upper fin are presented in Fig. 7. Qualitatively, very good agreement between the numerical and experimental results is achieved. The general shape of the curves is well matched. The location of the heat flux peaks induced by the injection bow shock is very accurately retrieved numerically. Moreover, the similarity between numerical and experimental heat flux values is very satisfactory except in the region closest to the fin shock (low Y values). Near the fin shock, the numerical heat flux shows an important overestimation. This is caused by the presence of the ‘numerical overestimation zone’ previously described. As seen in Fig. 6, the turbulent kinetic energy adjacent to the flat plate wall, near the fin shock, tends to be overestimated. This not only affects the regions unaffected by the injection bow shock, but also contributes to increase the value of the peaks within this region, as can be seen in Line A.

2. Flowfield description from numerical data

The heat flux distribution on the flat plate present an interesting feature consisting of a stripe of high heat flux approximately in the center of the vortex. This region extends from shortly downstream of the injection bow shock up to the end of the measurement region. This feature is difficult to visualize in the curves in Fig. 7, but it is apparent in the heat flux maps in Fig. 8. This high heat flux stripe is coupled with a neighboring low heat flux stripe, both highlighted in Fig. 9. Fig. 9 presents the numerical data showing the vortex-injection interaction flowfield.

Fig. 9a shows the evolution of the flow from upstream of the injector, to far downstream. The

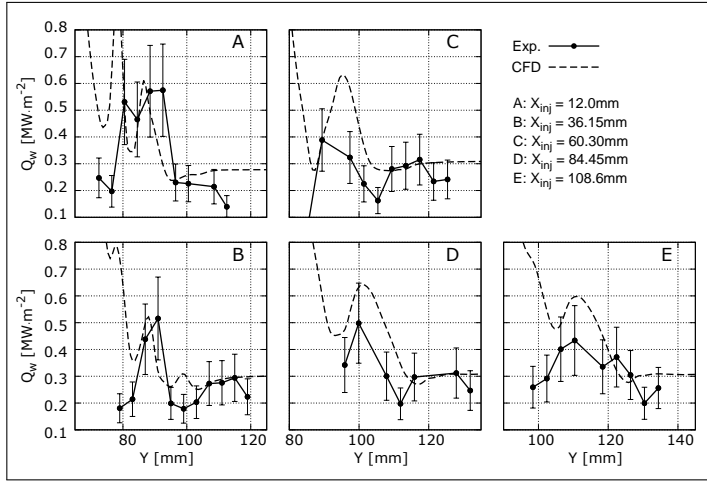


Fig. 7: Numerical and experimental heat transfer data. HI-UF (Case 1 in Table 2)

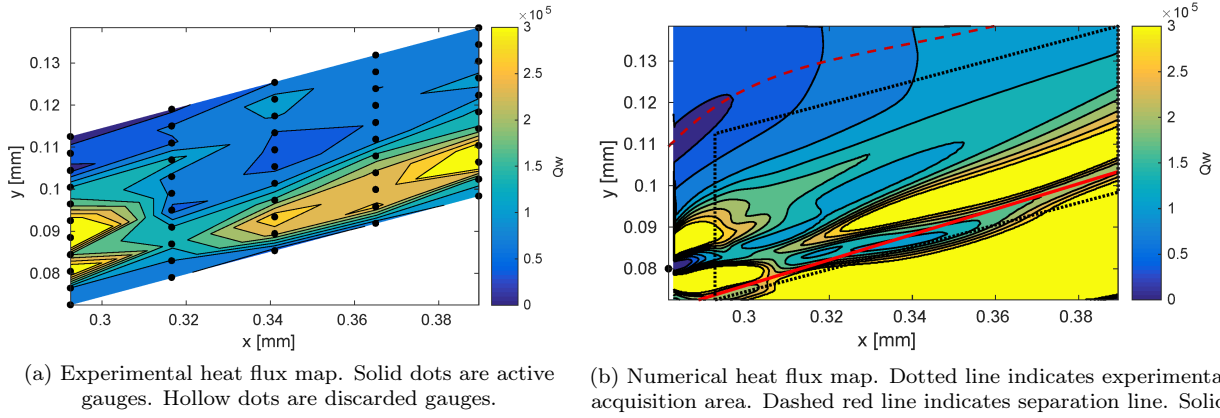


Fig. 8: Reconstructed heat transfer map. Comparison of heat flux from experiments and CFD. HI-UF (Case 3 in Table 2)

fuel plume evolves from a nearly hemispheric, to a highly elongated profile. Far downstream, the fuel plume splits in two regions, one located within the vortex recirculation region, and the other adjacent to the flat plate. The region of interest is presented in more detail in Fig. 9b. In this figure, the streak lines on the flat plate surface show the high and low heat flux stripes are coincident with a separation and a reattachment of the flow. The separation and reattachment lines are linked to the existence of a counter rotating vortex in this region. This vortex is shown in Fig. 9c, marked as ‘C.R. vortex’.

Despite the localized region of heat flux overprediction previously observed, the ability of the numerical methodology to accurately predict the location and extent of the counter-rotating vortex

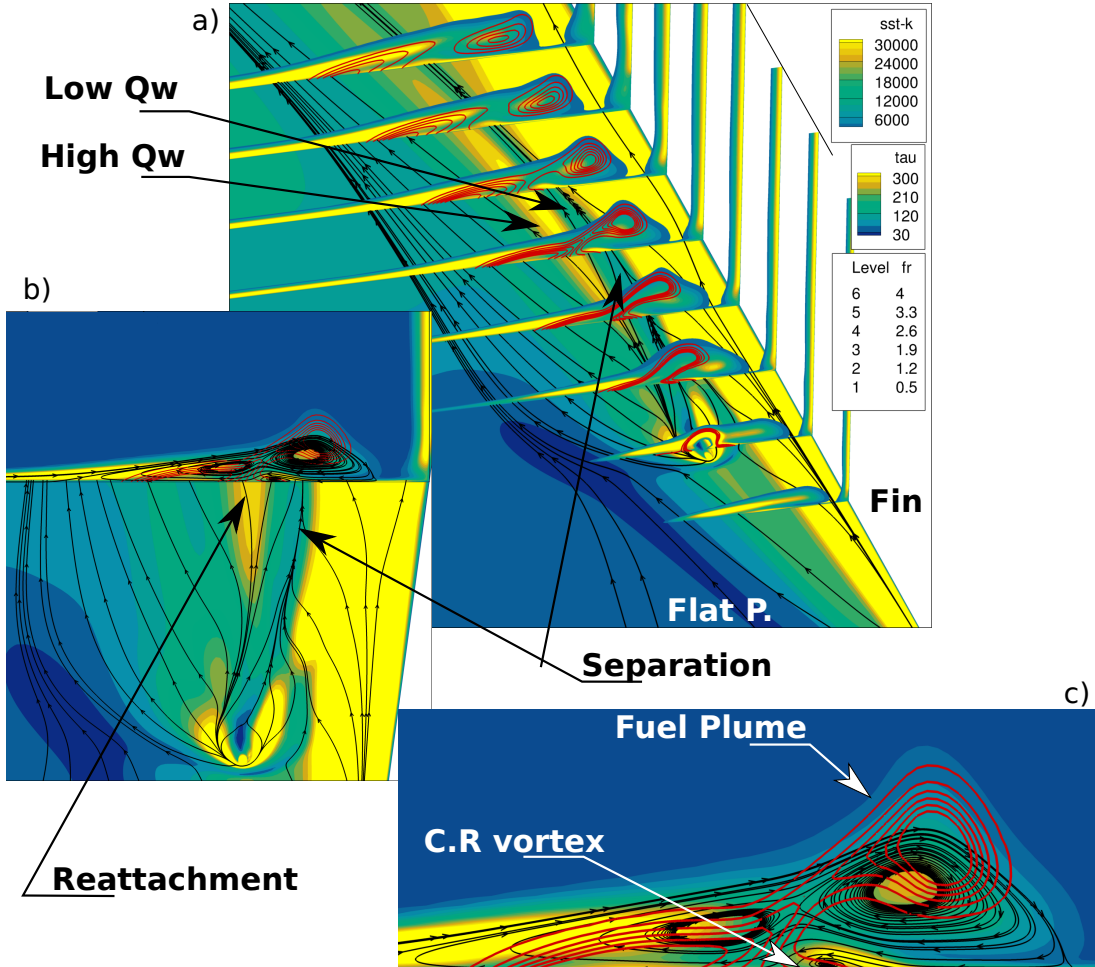


Fig. 9: Flat plate surface: numerical heat flux map with streak-lines. Slices: contours of turbulent kinetic energy, lines of equivalence ratio (red), and surface streamtraces. LP-HI-UF case.

within the main separation vortex indicates the 3-D flowfield is very accurately predicted.

3. Upper fin position, Low injection pressure

The case with low injection pressure shows very similar results to the high injection case. The location of the heat flux peaks is again very well predicted numerically. Moreover, the region far from the fin shock shows fairly good agreement in heat flux level. This can be observed in Fig. 10

Despite the similarities between the low and high injection cases, the low injection case shows a larger discrepancy between numerical and experimental data in the ‘numerical overestimation zone’.

In the high injection pressure case (HI-UF), the injection bow shock has a larger effect on heat flux, helping to mask the intrinsic error produced near the fin shock. In this case (LI-UF), the lower injection pressure makes the numerical error in the ‘numerical overestimation zone’ more

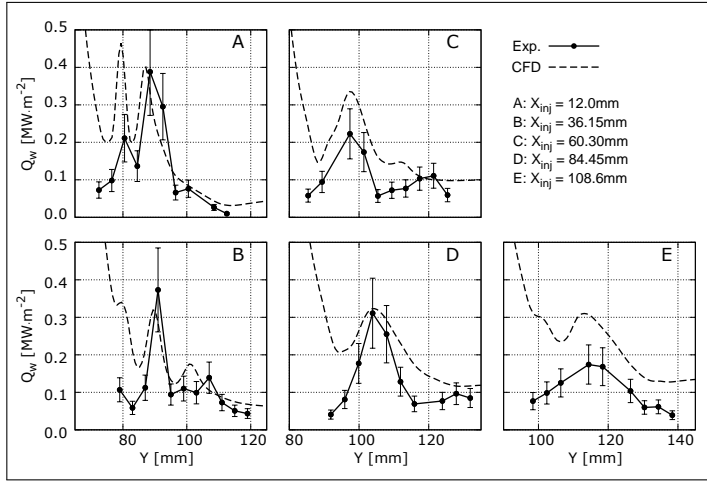


Fig. 10: Numerical and experimental heat transfer data. LI-UF (Case 2 in Table 2)

apparent. This is specially visible in lines A and E. In Line A, the left hand side peak is clearly overestimated due to its proximity to the fin shock. In Line E, the effect of the injection bow shock is substantially dissipated, incrementing the discrepancy between the lines due to effect of the ‘numerical overestimation zone’.

4. Lower fin position, High injection pressure

The heat flux results for the high injection pressure, low fin position (HI-LF) are presented in Fig. 11. These lines show very good agreement across the whole domain. This case shows a better agreement between the numerical and experimental data than the case with the Upper fin position. As previously described, the fin shock in the Lower fin position is further from the data acquisition region. Thus, a smaller area of the ‘numerical overestimation zone’ is affecting the measurements. This improvement is specially visible in Line A, where the experimental data points even for the left hand side peak lie very close to the numerical data line.

The agreement between the numerical and experimental heat flux data is very satisfactory. Not only the location of the heat flux peaks is well captured, but also the heat flux value is accurately predicted.

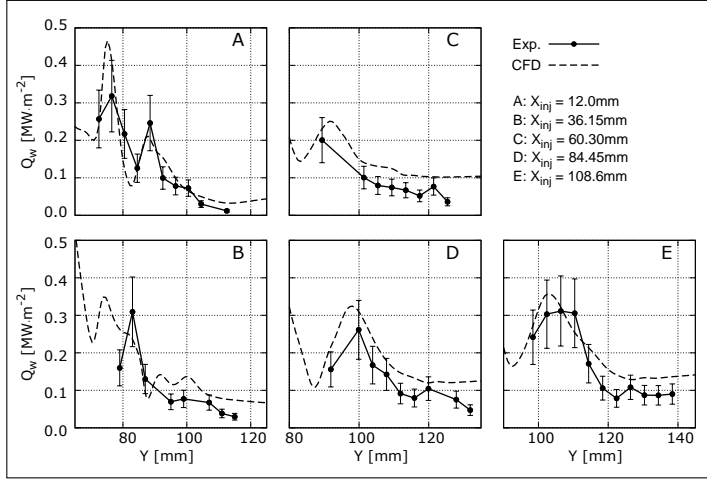


Fig. 11: Numerical and experimental heat transfer data. HI-LF (Case 3 in Table 2)

5. Lower fin position, Low injection pressure

The Lower fin Low injection case, low fin position heat flux data is presented in Fig. 12. Again, thanks to the fin shock sitting further from the measurement region, the effect of the ‘numerical overestimation zone’ is reduced compared to the high fin position case with Low injection pressure. Nonetheless, the accuracy of the numerical results is slightly lower than in the equivalent case with high injection pressure. As for the Upper fin cases, this is due to the lower effect of the injection bow shock on heat flux. This makes the tendency to overestimate heat flux near the fin in the numerical results more visible.

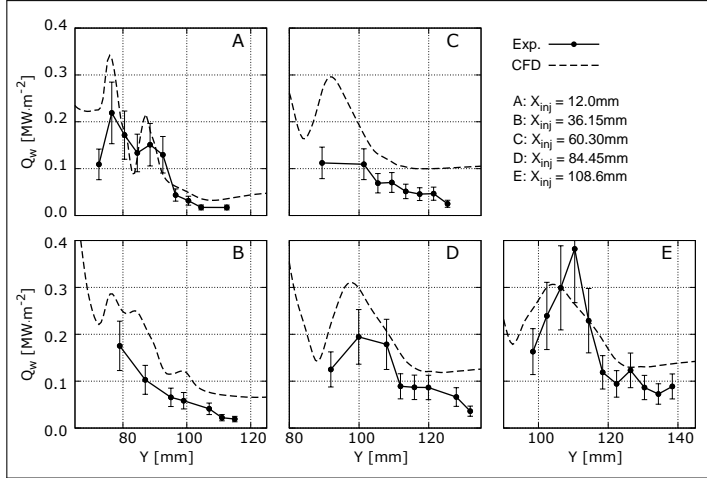


Fig. 12: Numerical and experimental heat transfer data. LI-LF (Case 4 in Table 2)

VII. Conclusions

A canonical geometry consisting of a flat plate plus fin with compression angle has been used to generate vortices representative of those intrinsically generated by scramjet inlets. By injecting within the vortex, the vortex-injection interaction and its effect on heat flux was studied. The data was obtained both experimentally and numerically, allowing to assess the ability of the numerical methodology to predict the experimental results.

The vortex measurements with no injection showed a localized region of severe mismatch between experimental and numerical data. This limitation of the numerical methodology was identified as a tendency to overpredict turbulent intensity by the $SSTk-\omega$ turbulence model on the flat plate surface in the region adjacent to the fin shock. The effect of the overprediction near the fin shock affects the numerical data also in the vortex-injection tests. This effect was found to be less severe as the fin shock is moved away from the data acquisition region by moving the fin.

Despite the limitations of the numerical methodology due to the local overprediction heat flux, the location of the injection bow shock and secondary counter-rotating vortex were very accurately retrieved. Moreover, the heat flux levels were satisfactorily accurate in the regions not adjacent to the fin shock. This suggests the flowfield is accurately predicted in by the numerical methodology.

VIII. Bibliography

- [1] Smart, M. K. & Tetlow, M. R., *Orbital delivery of small payloads using hypersonic airbreathing propulsion*, J. Spacecraft Rockets, **46**, No.1, 2009, 117-125.
- [2] Cook, S. & Hueter, U., *NASA's integrated space transportation plan 3rd generation reusable launch vehicle technology update*, Acta Astronautica, 53, 2003, 719-728.
- [3] Alvi, F. S. & Settles, G. S., *Physical model of the swept shock wave/boundary-layer interaction flowfield*, AIAA Journal, 30, No.9, 1992, 2252-2258.
- [4] Llobet, J. R., Gollan, R. J., & Jahn, I. H., *Scramjet inlet vortices: its effect on fuel plume elongation and mixing rate*, publication pending.
- [5] Llobet, J. R., Jahn, I. H. & Gollan, R. J., *Effect of stream-wise Vortices on Scramjets Porthole Injection Mixing*, Proceedings for the 20th AIAA International Space Planes and Hypersonic Systems and Technologies Conference, Glasgow, 2015.
- [6] Stalker, R .J., *The Free-Piston Shock Tube*, The Aeronautical Quarterly, 1965, 351-370.

- [7] Llobet, J. R., Barth, J. E. & Jahn, I. H., *Vortex Tracking Algorithm for Hypersonic Flow in Scramjets*, 19th AFMC, 8-11 December, Melbourne 2014. Submitted for publication.
- [8] Llobet, J. R., Jahn, I. H. & Gollan, R. J., *Effect of vortex-injection interaction on wall heat transfer in a flat plate with fin corner geometry*, Trans. JSASS Aerospace Tech. Japan, Vol.15, No.APISAT-2016, 2017, a17-a26.
- [9] Wise, D., *Experimental Investigation of a 3D Scramjet Engine at Hypervelocity Conditions*, PhD thesis, The University of Queensland, 2014.
- [10] Schultz, D. & Jones, T., *Heat-Transfer Measurements in Short-Duration Hypersonic Facilities*, AGARD-AG-165, North Atlantic Treaty Organization Advisory Group for Aerospace Research and Development, 1973.
- [11] Doherty, L., Zander, F. , Jacobs, P., Gollan, R., Chan, W., & Kirchhartz, R., *NENZF-r: Non-Equilibrium Nozzle Flow, Reloaded. A User Guide.*, Mechanical Engineering Report 2012/08, The University of Queensland School of Mechanical and Mining Engineering, 2012.
- [12] P. A. Jacobs, & R. J. Gollan., *The Eilmer3 Code: User Guide and Example Book.*, Mechanical Engineering Report 2008/07, The University of Queensland School of Mechanical and Mining Engineering, 2009.
- [13] P. A. Jacobs, R. J. Gollan, A. J. Denman, B. T. O'Flaherty, D. F. Potter, P. J. Petrie-Repar, & I. A. Johnston., *Eilmer's Theory Book: Basic Models for Gas Dynamics and Thermochemistry.*, Mechanical Engineering Report 2010/09, The University of Queensland School of Mechanical and Mining Engineering, 2010.
- [14] McBride, B. J., & Gordon, S., *Computer program for calculation of complex chemical equilibrium compositions and applications. Part 2: User manual and program description.*, Reference Publication 1311, NASA, 1996.